



Yolk-shell nanovesicles endow glutathione-responsive concurrent drug release and T_1 MRI activation for cancer theranostics

Dahai Liu^a, Zijian Zhou^b, Xinyu Wang^a, Hongzhang Deng^b, Lin Sun^c, Haixin Lin^d, Fei Kang^b, Yong Zhang^b, Zhantong Wang^b, Weijing Yang^b, Lang Rao^b, Kuikun Yang^b, Guocan Yu^b, Jianshi Du^{a,*,**}, Zheyu Shen^{e,***}, Xiaoyuan Chen^{b,*}

^a Lymph and Vascular Surgery Department, China-Japan Union Hospital of Jilin University, Changchun, Jilin, 130033, China

^b Laboratory of Molecular Imaging and Nanomedicine, National Institute of Biomedical Imaging and Bioengineering, National Institutes of Health, Bethesda, MD, 20892, United States

^c Department of Materials Science and Engineering, International Institute for Nanotechnology, Northwestern University, Evanston, IL, 60208, United States

^d Department of Chemistry, International Institute for Nanotechnology, Northwestern University, Evanston, IL, 60208, United States

^e Guangdong Provincial Key Laboratory of Construction and Detection in Tissue Engineering, Biomaterials Research Center, School of Biomedical Engineering, Southern Medical University, Guangzhou, 510515, China

ARTICLE INFO

Keywords:

Nanovesicles
Metal-drug coordination
MRI
Iron oxide
Concurrent theranostics

ABSTRACT

The effort of incorporating therapeutic drugs with imaging agents has been one of the mainstreams of nanomedicine, which holds great promise in cancer treatment in terms of monitoring therapeutic drug activity and evaluating prognostic index. However, it is still technically challenging to develop nanomedicine endowing a spatiotemporally controllable mechanism of drug release and activatable imaging capability. Here, we developed a yolk-shell type of GSH-responsive nanovesicles (NVs) in which therapeutic drug (Doxorubicin, DOX) and magnetic resonance imaging (MRI) contrast agent (ultrasmall paramagnetic iron oxide nanoparticles, USPIO NPs) formed complexes (denoted as USD) and were encapsulated inside the NVs. The formation of USD complexes is mediated by both the electrostatic adsorption between DOX and poly(acrylic acid) (PAA) polymers and the DOX-iron coordination effect on USPIO NPs. The obtained USD NVs showed a unique yolk-shell structure with restrained drug activity and quenched T_1 MRI contrast ability which, on the other hand, can respond to glutathione (GSH) and lead to drug release and T_1 contrast activation in a spatiotemporally concurrent manner. Furthermore, the USD NVs exhibited great potential to kill HCT116 cancer cells *in vitro* and effectively inhibit the tumor growth *in vivo*. This study may shed light on the design of sophisticated nanotheranostics in precision nanomedicine.

1. Introduction

Molecular drugs usually suffer from poor biodistribution *in vivo* which greatly hinders the effectiveness of therapeutic drugs in disease treatment [1]. The past decades have witnessed tremendous advances in nanomedicine which have provided great versatility and feasibility in revolutionizing traditional disease treatments [2]. Multifunctional nanomaterial platforms implicating the physiochemical properties of polytropic nanomaterials have gained momentum [3–5], which hold great promise in disease diagnosis, treatment, therapeutic monitoring, and prognosis [6,7]. Drug delivery system (DDS) is ideally conducted with targeted delivery and controlled release of therapeutic agents

[8,9]. Engineering nanomaterials as drug delivery vehicles opens up a new era of DDS by tailoring the delivery and targeting approaches for improved therapeutic outcomes [10,11]. Besides passive (e.g., enhanced permeability and retention effect, EPR) and active (e.g., antibody or peptide interactions) targeting strategies [12,13], stimuli-responsive systems enabling on-demand drug release may achieve enhanced drug accumulation in desired tissues and reduced systemic toxicity to healthy tissues [14,15]. For example, the relatively low-pH milieu, arising from the fast glucose metabolism of most tumors, has spurred the design considerations of pH-responsive systems for tumor-specific imaging and cancer therapy [16–19]. Glutathione (GSH) is one of the most abundant antioxidants in living organisms which is

* Corresponding author.

** Corresponding author.

*** Corresponding author.

E-mail addresses: dujianshi3043@163.com (J. Du), sz@smu.edu.cn (Z. Shen), shawn.chen@nih.gov (X. Chen).

revolutionized to an elevated level in most cancers during the tumor progression and metastasis. The exploitation of GSH-responsive nanomaterials has been widely recognized to facilitate controllable drug release, which holds great promise for precision nanomedicine [20–24].

On account of monitoring drug release, the physiological fate of administered drugs is of paramount importance in terms of locating drug distribution, reporting drug activity, and finally improving the therapeutic efficacy [25,26]. To this end, cancer theranostics integrating both therapeutic drugs and imaging agents have emerged as an important frontier in nanomedicine [27–29]. Nanomaterials can be easily engineered as vehicles to load both therapeutic drugs and imaging agents. However, one caveat here is that the imaging agents and therapeutic drugs may have different pharmacokinetics and biodistribution patterns *in vivo* due to premature release or accidental decomposition [9,30], which dampens the rationality of monitoring the drug release through imaging results. Therefore, an ideal system should be operated with a spatiotemporally concurrent feature for both the imaging agents and the therapeutic drugs, in which therapeutic drug release is accompanied by imaging through a single stimulus [31,32]. Based on these design considerations, cancer theranostics with activatable imaging and drug releasing profiles in a concurrent manner may be a promising platform for improving prognostic prediction and therapeutic outcomes [33,34]. Recently, a variety of activated imaging techniques has been implicated in nanomedicine to monitor drug release and screen drug activity [35–41]. However, it is still synthetically demanding and technically challenging to integrate the two processes in a concurrent manner due to the difficulty in identifying a single mechanism eligible to activate both drug release and imaging.

Due to the high stability, flexible lateral fluidity and heterogeneity of polymersomes over liposomes, polymersome nanovesicles (NVs) have gained momentum to be utilized as versatile platforms for improved cancer theranostics [42]. Herein, we report a novel design of using polymersome NVs as concurrent theranostics in which the drug release and the turn-on effect of T_1 magnetic resonance imaging (MRI) signal are stimulated by a single mechanism of GSH-triggered decomposition of the NVs. The NVs are formed by self-assembly of poly(ethylene glycol)-poly(propylene sulfide)-SS-poly(ethylene glycol) (PEG-PPS-SS-PEG) amphiphilic triblock copolymers through a thin-film hydration method (Fig. 1A). During the self-assembly process, theranostic agents (denoted as USD complexes), composed of ultra-small paramagnetic iron oxide nanoparticles (USPIO NPs) and doxorubicin (DOX), are encapsulated into the inner space of the NVs to attain USD NVs. The as-synthesized USPIO NPs are coated with poly(acrylic acid) (PAA) polymers which interact with DOX to form USD complexes through electrostatic interaction and metal-drug coordination effect. MRI is widely used in clinical diagnosis due to the non-invasive and non-radiation characteristics, and more importantly, enabling high spatial resolution especially on soft tissues (e.g., solid tumors). Responsive MRI systems can be achieved through engineering the parameters that influence the T_1 and T_2 relaxivities of magnetic nanomaterials [43,44]. For example, the chemical exchange between water molecules and magnetic centers is likely the most important factor for T_1 relaxation enhancement [45,46], so that excluding water molecules from magnetic centers could lead to dormant T_1 effect and *vice versa* [47,48]. In the current work, the formation of USD complexes results in “quenching” of the T_1 MRI contrast of USPIO NPs due to the restricted water penetration and the elevated T_2 shortening effect of the system [48–51]. Upon cellular internalization and exposure to GSH, the cleavage of disulfide bonds destabilizes the USD NVs, leading to reverse micellation and release of the USD cargos (Fig. 1B) [52]. Although there have been many reports of MRI-monitored drug release studies, very few of them elaborated on designing a single mechanism that is responsible for both MRI activation and drug release in a current manner. Our work reports a spatiotemporally concurrent process of both T_1 MRI activation and therapeutic drug release, which may shed light on designing theranostic biomaterials in precision nanomedicine.

2. Experimental section

2.1. Preparation of ultrasmall paramagnetic iron oxide nanoparticles

The USPIO NPs were prepared by a published procedure in our previously report [53]. Briefly, 80 mg of PAA (Mw = 1800) was dissolved in 20 mL of DI water and purged with nitrogen before heated to reflux. 0.4 mL of a mixed solution of iron precursors (1 M FeCl_3 and 0.5 M FeSO_4) was quickly injected into the hot solution followed by the addition of 6.0 mL of ammonia solution. The solution was kept at the reflux temperature for 1 h before cooling to room temperature. The solution was further dialyzed in water to remove excess of surfactants. The USPIO NPs solution was stored at room temperature for further use.

2.2. Synthesis of PEG-PPS-SS-PEG amphiphilic triblock polymers

Poly(ethylene glycol) methyl ether (mw 750) were used as source materials to obtain PEG-Tosyl and PEG thioacetate according to previously reported procedures (Fig S1, i and ii). The obtained PEG thioacetate was transformed into PEG-PPS-disulfide pyridine according to following procedure: 4 mL of THF was used to dissolve 200 mg of PEG thioacetate and the system was degassed with N_2 . 16 mg of sodium methoxide were dissolved in 0.5 mL of MeOH (0.5 M) and added to the flask through syringe and left for 30 min. After then, propylene sulfide (750 mg, 40 eq.) were injected to the system through syringe. The system was left to react for 45 min before adding 165 mg of disulfide dipyridine in THF and left overnight. The product was collected by precipitation in ethyl ether for three times and dried under vacuum. The product PEG-PPS-disulfide pyridine (300 mg) were then dissolved in THF and HS-PEG- NH_2 (mw 1k, 160 mg) was added for conjugation. The reaction was left for 48 h and the final product was collected and dried under vacuum. The product from each step was dissolved in CDCl_3 and characterized by ^1H NMR spectroscopy (Bruker, 300 MHz).

2.3. Raman measurement

To collect Raman spectra, the samples were placed on a glass slide (1 mm Micro slide from Fisherbrand). The thickness of the samples is around tens of micron. The Raman spectra were collected with a Raman microscope (Witec Alpha300R confocal microscope, Germany) with a 785-nm excitation line under a 50x dark-field lens in reflection mode. Each spectrum is collected by accumulating 50 measurements with 2 s irradiation.

2.4. Preparation of nanovesicles

The NVs of different formulations were formed through the thin-film hydration method. Briefly, 6 mg of PEG-PPS-PEG copolymers were dissolved in 1.0 mL of CHCl_3 in a 25 mL flask. The solution was left in chemical hood to allow the evaporation of the solvent which was further removed by vacuum for 30 min. For the preparation of blank NVs, 0.5 mL of deionized (DI) water was added to the flask to hydrate the thin film on the flask for 20 min. The solution was further applied with sonication for 15 min until the formation of a cloudy solution. The solution was further purified by centrifugation at 4000 rpm to remove any possible precipitations and stored at room temperature for further use. For the preparation of DOX NVs, 0.5 mL of DOX (1 mg/mL) dissolved in DI water was added to the flask following a similar procedure as above. The final solution was purified by dialysis against water for 3 days with multiple changes of outside solvent. For the preparation of US NVs, 0.5 mL of PAA coated USPIO NPs was added to the flask and underwent sonication for 15 min. The solution was further purified by removing free USPIO NPs through centrifugation. For the preparation of USD NVs, the USPIO NPs (1 mg/mL) and DOX (1 mg/mL) solutions were mixed immediately before dropwise adding into the thin-film flask. The procedure was accompanied with sonication to prevent

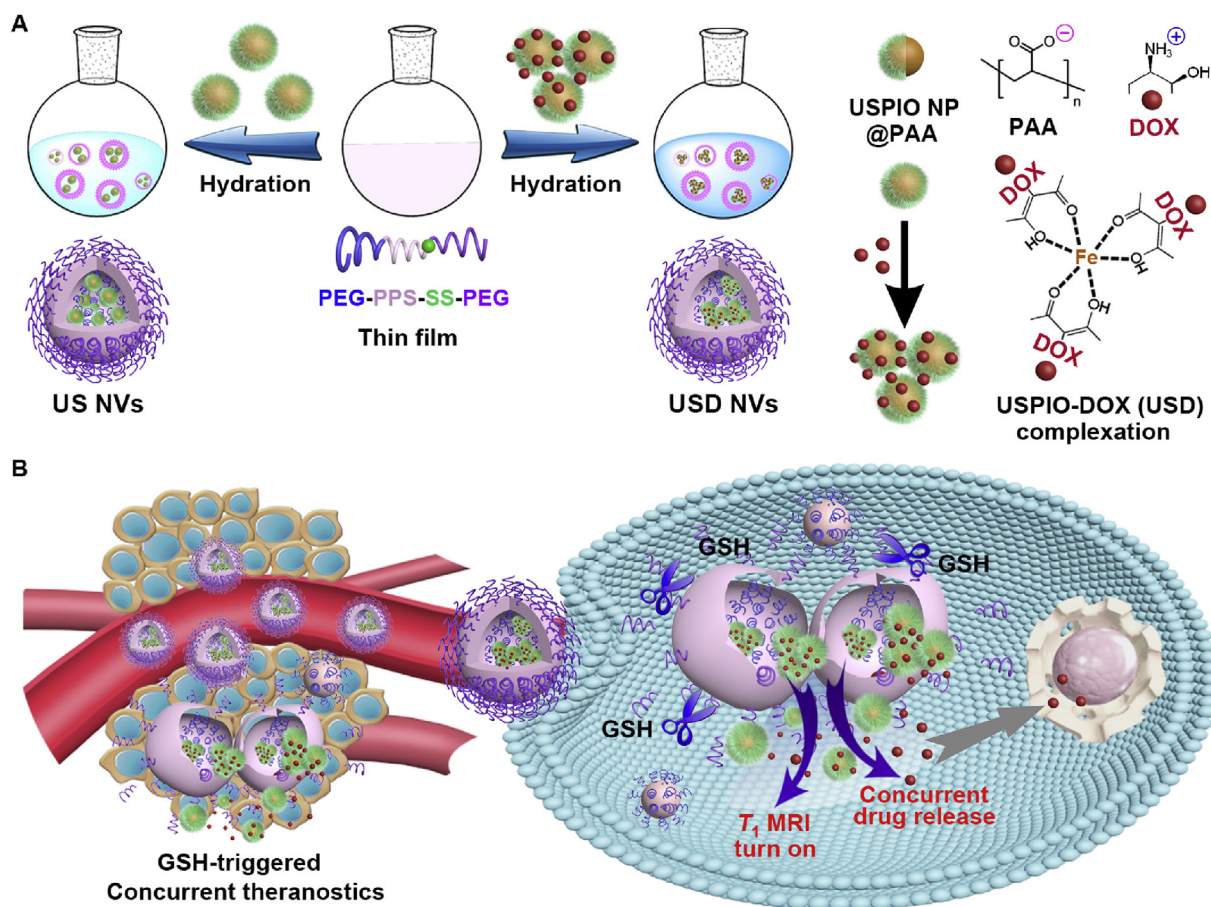


Fig. 1. Schematic illustration of the concurrent nanotheranostics. (A) Poly(acrylic acid) (PAA) coated ultrasmall paramagnetic iron oxide nanoparticles (USPIO NPs) interact with doxorubicin (DOX) forming USD complexes mediated by both the electrostatic absorption between DOX and PAA polymers and the DOX-iron coordination effect on USPIO NPs. During the nanovesicles (NVs) formation by self-assembly of poly(ethylene glycol)-poly(propylene sulfide)-SS-poly(ethylene glycol) (PEG-PPS-SS-PEG) amphiphilic triblock copolymers through a thin-film method, either USPIO NPs or USD complexes are added to form US NVs or USD NVs, respectively. (B) After tumor accumulation and cell internalization, the USD NVs are decomposed under GSH environment which lead to drug release and T_1 MRI activation phenomenon in a spatiotemporally concurrent manner.

precipitation of the USD complexes. The solution was further purified by centrifugation to remove large precipitations and stored at room temperature for further use.

2.5. Cell viability assay

The cell viability was evaluated by MTT (3-[4,5-dimethylthiazole-2-yl]-2,5-diphenyltetrazolium bromide) assay on two cell models, HCT116 and A549. Cells were first seeded in a 96-well plate at 1×10^4 cells/well and incubated at 37 °C for 24 h. The NVs of different formulations and of different concentrations were added to the wells, and further incubated for 48 h before conducting the standard MTT procedure. The cell viability was derived from the Uv-vis absorption at 570 nm according to the following equation: [(Absorption of sample - absorption of background)/(absorption of control - absorption of background)] * 100%. Data represents to mean \pm s.d. (n = 3).

2.6. MRI measurements

The MRI study was conducted on a 7 T scanner (Bruker). The phantom samples with different Fe concentrations were prepared containing acquired amount of GSH. The T_1 MRI phantom study was conducted using rapid acquisition with relaxation enhancement with variable repetition time (RARE-VTR) sequence by the following parameters: Multiple Repetition Time = 50, 250, 500, 1000, 2000, 4000, 6000 ms, Echo Time = 12.507 ms, Effective TE = 12.507 ms, Number

of Experiments = 7, Rare Factor = 2, Number of Repetitions = 1, Number of Averages = 1, Flip Angle = 180, Matrix = 256 \times 256. The T_2 MRI phantom study was conducted using multi-slice multi-echo (MSME) sequence by the following parameters: Repetition Time = 2000 ms, Echo Time = 10 ms, Effective TE = 10, 20, 30, 40, 50, 60, 70, 80, 90, 100, 110, 120, 130, 140, 150, 160 ms, Number of Repetitions = 1, Number of Averages = 1, Flip Angle = 180, Matrix = 256 \times 256. The data was handled by Image J and analyzed with the MRI Analysis and Calculator plugin to obtain the T_1 and T_2 relaxation time for each sample.

2.7. In vivo MRI of mouse tumors

The *in vivo* MRI of subcutaneous tumors was conducted on a 7 T scanner (Bruker). All animal experiments were performed under the National Institutes of Health Clinical Center Animal Care and Use Committee (NIH CC/ACUC) approved protocol. Mice were anaesthetized by isoflurane (1.0–2.0%) in oxygen and placed in an animal-specific body coil for data acquisition. The multi-slice T_1 MRI was acquired with RARE sequence using the following parameters: Repetition Time = 350 ms, Echo Time = 10.3 ms, Effective TE = 10.3 ms, Rare Factor = 2, Flip Angle = 180, Number of Repetitions = 1, Number of Experiments = 1, Number of Averages = 8, Matrix = 256 \times 256. The data was finely analyzed by Image J to obtain the signal intensity for region-of-interest of tumor and semi-quantitative analysis of the SNR and CNR of tumor.

2.8. Cancer therapy study on HCT116 tumor model

All animal experiments were performed under the National Institutes of Health Clinical Center Animal Care and Use Committee (NIH CC/ACUC) approved protocol. The HCT116 mouse tumor model was established by subcutaneously injecting 2×10^6 of HCT116 cells into the right back flank of each mouse (Athymic nude, Envigo, USA). After the tumor size reached around 40–50 mm³, mice were randomly grouped into 6 groups (n = 5). Mouse groups were treated with different formulations: PBS, free DOX, US NVs, DOX NVs, USD NVs + BSO and USD NVs, respectively. Each group contains four doses at every three days. Each dose represents to 4 mg DOX per kg mouse body weight or equivalent components in different formulations. At the first time treatments, the mouse groups treated with US NVs, USD NVs + BSO and USD NVs were subjected to MRI study by multi-slice T₁-weighted MRI sequence as described elsewhere. The tumor size and body weight for each mouse groups were recorded every two days after starting the first treatment. The mouse survival rates for each mouse groups were recorded until 35 days after the first treatment. The mouse tumor volume was calculated by the equation: $V = \text{width}^2 \times \text{length}/2$. The quantitative tumor inhibition ratios in percentage (%) at the day 20 are calculated by the following equation: $(1 - ((\text{exp}_{\text{day}20} - \text{exp}_{\text{day}0}) / (\text{control}_{\text{day}20} - \text{control}_{\text{day}0}))) * 100$.

3. Results and discussion

We first synthesized the triblock PEG-PPS-SS-PEG copolymers through a modified procedure from literature (Fig. S1) [54]. The formation of triblock PEG₇₅₀-PPS-SS-PEG₁₀₀₀ copolymer was confirmed from the integration analysis of the proton nuclear magnetic resonance (¹H NMR) spectrum (Figs. S2 and S3). The Raman spectroscopy shows a characteristic Raman shift at around 521 cm⁻¹ for the disulfide bond, further confirming the formation of triblock copolymer (Fig. S4). The success of liposomal drugs (e.g., Doxil® and Onivyde®) in the treatment of cancers have spurred great interest in exploring polymersomes as drug delivery platforms for cancer theranostics [42,55,56]. The synthesized triblock copolymers can form uniform NVs (denoted as block NVs) with size around 70–90 nm (Fig. S5), which is similar to that of previously reported results[33]. We further prepared PAA-coated USPIO NPs by a well-controlled hydrothermal method, which showed an average diameter of 3–4 nm from the transmission electron microscopy (TEM) and the high-resolution TEM image (Fig. 2A), indicating great potential to serve as efficient T₁ contrast agents [53,57,58]. Due to the presence of PAA polymers on the surface, the as-synthesized USPIO NPs had an intrinsic pH value of around 4.5 when dispersed in DI water. It should be noted that the PAA-coated USPIO NPs were stable in solution without obvious precipitation or dissolution over several months [53].

We found that USD complexes can be formed by directly mixing USPIO NPs and DOX solutions. This phenomenon is possibly due to two factors: first, the electrostatic adsorption between PAA and DOX; second, the coordination effect between iron ions on nanoparticle surface and the anthracene rings of DOX molecules. Each iron(III) ion may coordinate with three DOX molecules according to previous spectroscopic studies [59,60]. The Fourier transform infrared (FTIR) spectrum further confirmed the formation of metal-DOX complexes with a weak N–H stretching peak at around 3450 nm and a broadened O–H stretching peak at around 3450–3250 cm⁻¹ (Fig. S6). The USD complexes dispersed well in water with a weight ratio of 1:1 for USPIO NPs to DOX, attaining a spheroidal shape with diameters ranging from 50 to 80 nm according to the TEM image (Fig. 2B). Furthermore, increasing the weight ratio of USPIO NPs to DOX from 1:1 to 2:1, 3:1, 4:1, and 5:1 resulted in obvious turbulence which could be precipitated under centrifugation (Fig. 2C). More importantly, the presence of GSH (5 mM, pH 7.4) could readily decrease the hydrodynamic size of the USD complexes as monitored by dynamic light scattering (DLS)

measurements (Fig. S7).

We further showed that the USPIO NPs can be encapsulated into the NVs, denoted as US NVs (Fig. 2D). Although the average encapsulation efficiency was measured to be about 46.7%, the purification of US NVs from the USPIO NPs could be easily conducted by centrifugation due to the excellent dispersion ability of single USPIO NPs in solution. The formation of USD NVs was similar to that of US NVs except for the use of USD solution as feeding materials with the USPIO:DOX weight ratio of 1:1. In a typical procedure, the loading capacity of DOX to the overall weight of USD NVs was calculated as 14.3%, which was about 30% higher than that of the commercial Doxil liposomes (DOX content: 11.1%). Further increasing the loading capacity of USD NVs was also possible, however, the self-assembly procedure may suffer from significant drop of loading efficiency due to the inevitable formation of micelles rather than polymersomes. Hereafter, we used the USD NVs with DOX loading capacity of 14.3% for further *in vitro* and *in vivo* studies. The TEM image of the USD NVs showed an interesting yolk-shell structure in which the yolk was the US complexes and the shell was the PPS membrane (Fig. 2E–G). DLS analysis results showed that the hydrodynamic diameters of US NVs and USD NVs were 107.6 ± 23.2 and 153.7 ± 36.4 nm, respectively (Fig. S8). Furthermore, we prepared free DOX loaded polymersomes, denoted as DOX NVs, which showed a hydrodynamic diameter of about 112.7 ± 29.5 nm, similar to that of blank NVs (Fig. S9). It is of note that the maximum drug loading capacity of the DOX NVs under an optimized condition was 4.6% which was about 3-fold lower than that of the USD NVs, underscoring the great necessity and feasibility of forming USD complexes for improved drug loading efficiency.

To investigate the GSH-triggered drug release profiles, we incubated the USD NVs in phosphate buffer solution (pH 7.4) in the presence and absence of GSH at a concentration of 5 mM. The DOX NVs were used as a control sample under the equivalent conditions. The drug release was quantified through the fluorescence measurement of DOX. The bare USD complexes showed a quick release of DOX, 37.6% in the first hour and 83.1% at 24 h, due to the instability of the USD complexes under neutral condition (Fig. 3A). However, the USD NVs had less than 20% drug release within 24 h, indicating that the vesicular formulation was able to protect the inside USD complexes from dissociation. Furthermore, the addition of GSH to the USD NVs resulted in an efficient release of DOX while maintaining other conditions as the same, 33.1% at 1 h and 63.4% at 24 h, which gradually reached 74.3% at 72 h. The releasing profiles are similar to that of DOX NVs with and without GSH, respectively, indicating that GSH is responsible for triggering the decomposition of these NVs and facilitating the drug release.

Meanwhile, we studied the MRI performance of the US NVs and the USD NVs in the presence and absence of GSH. The T₁ MRI phantom results were acquired with different sample concentrations of 0.4, 0.2, 0.1, 0.05, 0.025 mM, with respect to Fe ions. Compared with the US NVs and the USD NVs only, the GSH treatment led to prominently enhanced T₁ bright contrast with increased sample concentrations, respectively (Fig. 3B). Furthermore, we found that the USD NVs in the absence of GSH showed slightly dark contrast with increased concentrations in the T₁ MRI probably due to the elevated T₂ shortening effect. The r₁ relaxivity values of the US NVs and the USD NVs were significantly increased (**p < 0.001) in the presence of GSH by a factor of about 2 and 13, from 1.7 ± 0.3 and 0.2 ± 0.04 to 3.1 ± 0.4 and 2.7 ± 0.4 mM⁻¹s⁻¹, respectively (Fig. 3C). The r₂ relaxivity value showed a sharp decrease for the USD NVs + GSH compared with that of USD NVs only, from 37.4 ± 4.3 to 26.3 ± 5.1 mM⁻¹s⁻¹ (Fig. S10). In contrast, the US NVs showed slightly increased r₂ values from 18.6 ± 2.3 to 23.7 ± 3.4 mM⁻¹s⁻¹ upon incubation with GSH under the same conditions as above. This phenomenon could be ascribed to the interplay between the T₁ and T₂ relaxation enhancement effect upon the formation of USD or USD NVs. The aggregation of USPIO NPs may prohibit the water penetration and the chemical exchange between water molecules and paramagnetic centers on the surface, which

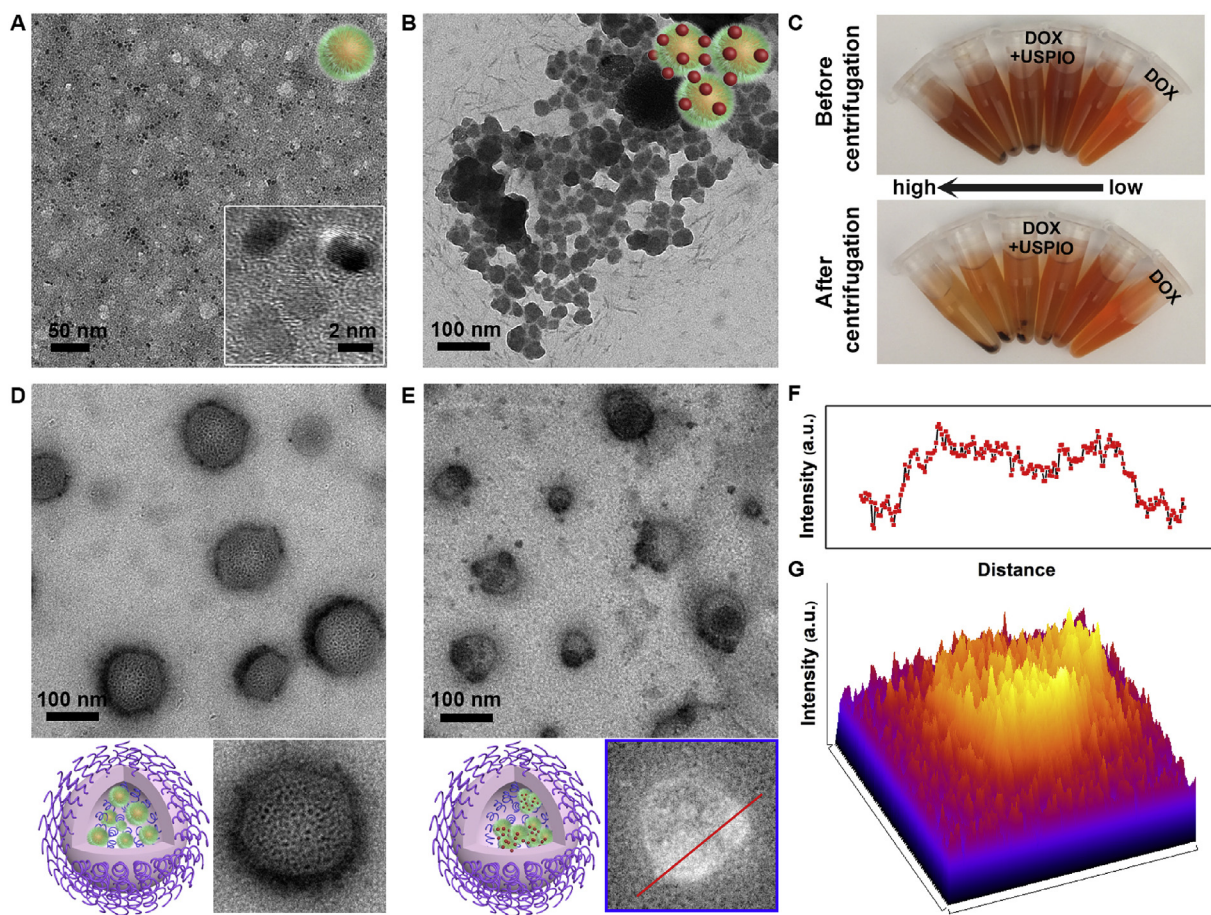


Fig. 2. Characterization of nanoparticles and nanovesicles. (A) TEM image, high-resolution TEM image (inset, lower), and cartoon (inset, upper) of the USPIO NPs. (B) TEM image and cartoon (inset) of the USD complexes. (C) Photographs of the formation of USD complexes by mixing PAA coated USPIO NPs and DOX in water. Arrow indicates the concentration of USPIO NPs from low to high, with weight ratio between USPIO NPs and DOX ranging from 0:1 to 1:1 2:1, 3:1, 4:1, and 5:1. (D) TEM image, high-resolution TEM image (lower right) and cartoon (lower left) of US NVs. (E) TEM image, intensity reversed high-resolution TEM image (lower right) and cartoon (lower left) of USD NVs. (F, G) Line (red) and surface profile of the intensity from the high-resolution TEM image of the USD NVs, respectively. (For interpretation of the references to color in this figure legend, the reader is referred to the Web version of this article.)

reduces the T_1 relaxation enhancement effect. Moreover, the aggregation effect results in an enhanced magnetic field coupling effect between USPIO NPs which may largely augment the T_2 shortening effect of the USD NVs. Taken together, both the decreased T_1 effect and increased T_2 effect contribute to the T_1 “quenching” effect in the USD NVs. The similar phenomenon was also found when comparing the T_1 and T_2 relaxivities of the USD complexes and the USPIO NPs, respectively (Fig. S11).

The TEM images showed that the USD NVs fused with each other in the presence of GSH after incubation for 1 h, which was attributed to the instability induced by the GSH cleavage of PEG chains on the vesicular surface (Fig. 3D and E). At 2 h time point, most of the USD NVs were decomposed with clear observation of individual USPIO NPs due to the reverse micellation process and dissociation of the USD complexes. In addition, the vesicular structure disappeared from the TEM images at 4 h. The DLS results of the USD NVs + GSH revealed a slight increase of the hydrodynamic size at initial incubation time and a sharp drop at 24 h, which should be ascribed to the fusion-mediated reverse micellation process (Fig. S12). These results are consistent with the drug releasing profiles described above.

To investigate the drug releasing profiles *in vitro*, we studied the cellular fate of USD NVs, DOX NVs, and free DOX, and the fluorescence of DOX was measured by confocal microscopy. L-buthionine sulphoximine (BSO) is an inhibitor of gamma-glutamylcysteine synthetase which consequently lowers the intracellular GSH concentration. Hence,

we studied the cellular fate of USD NVs + BSO and DOX NVs + BSO as control groups. We hypothesized that the GSH-mediated DOX release from the USD complexes led to the recovery of the fluorescence, which otherwise was largely quenched due to the presence of USPIO NPs. The results showed that both DOX NVs and USD NVs had remarkable fluorescence signal from cell nucleus which could be attributed to DOX release and intrinsic tropism to cell nucleus (Fig. 4A). In contrast, the fluorescence signal was weaker in the USD NVs + BSO and DOX NVs + BSO groups under the similar conditions, which were compared semi-quantitatively and summarized in the Fig. 4B. The relatively low DOX intensity for the free DOX group (i) compared with DOX NVs (ii) and USD NVs (iv) could be due to the efflux transportation effect of free DOX by cells, indicating the possible different cellular uptake efficiency and kinetics of different formulations. We further used flow cytometry to investigate the reactive oxygen species (ROS) generation in cells treated with different formulations (Fig. 4C). The results showed that the USPIO NPs did not increase the intracellular ROS generation, which could be ascribed to the low cellular uptake of the negatively charged USPIO NPs. However, the USD NVs attained a significantly increased ROS level compared with control and DOX only treatment groups. Furthermore, the addition of BSO decreased the intracellular ROS generation by USD NVs, probably due to the reduced release of drugs. It is noteworthy that the presence of both USPIO NPs and DOX cooperatively increased the intracellular oxidative stress which may serve as a lethal factor to cells [61,62].

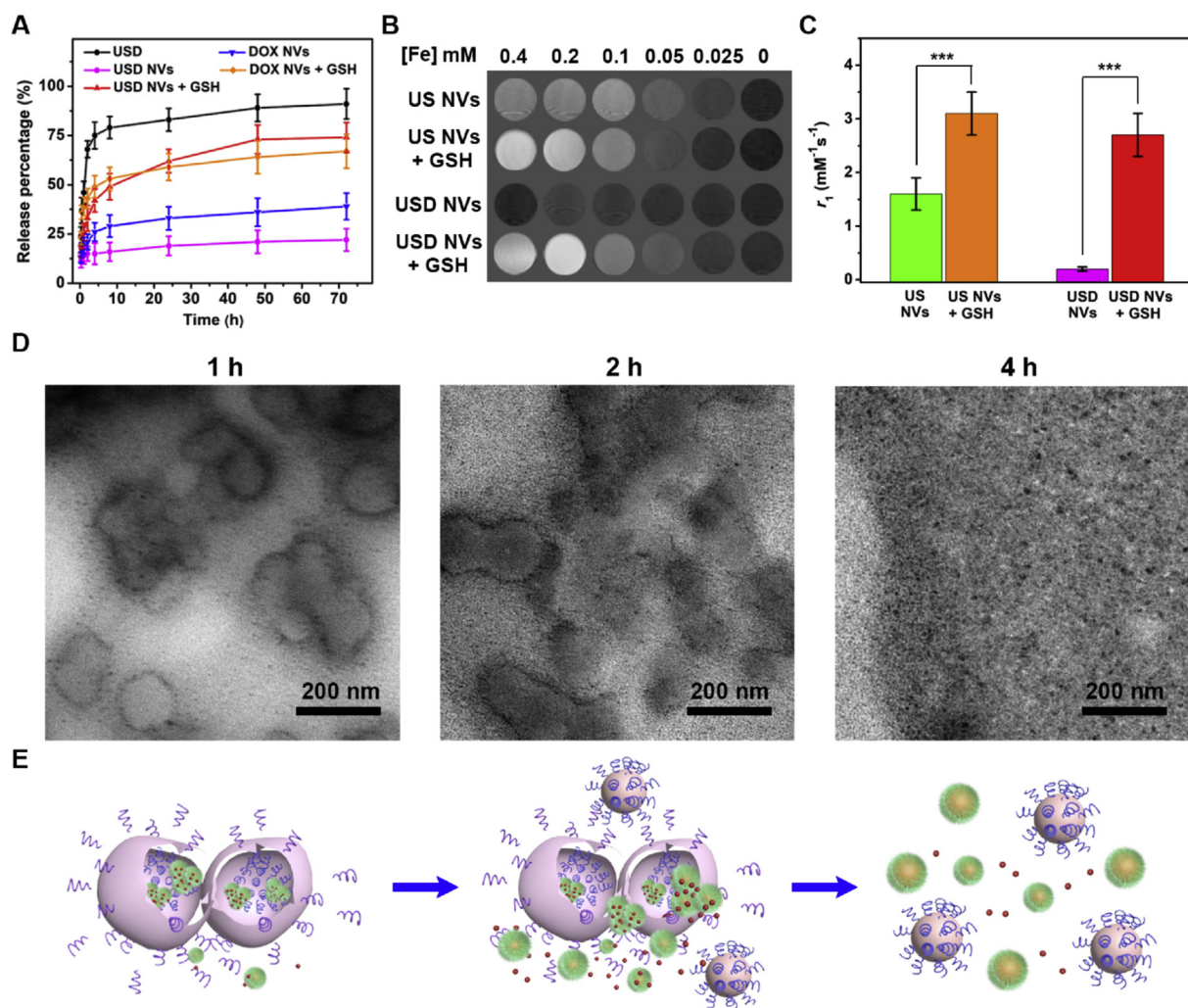


Fig. 3. GSH-triggered drug release and MRI turn-on phenomenon of the USD NVs. (A) Drug releasing profiles of USD complexes, USD NVs, and DOX NVs with and without GSH (5 mM) incubation. The drug releasing percentages were measured based on DOX fluorescence. (B, C) MRI phantom and r_1 values of US NVs and USD NVs with and without GSH (5 mM) incubation, respectively. Samples with different concentrations were prepared normalized to Fe elements. *** $p < 0.001$. (D, E) TEM images and cartoon illustrations of the USD NVs incubated with GSH for different time, respectively.

The cytotoxicity study was evaluated on both human colorectal carcinoma HCT116 and lung cancer A549 cell models. We used 3-[4,5-dimethylthiazole-2-yl]-2,5-diphenyltetrazolium bromide (MTT) assay to evaluate the cell viability after treatment with free DOX, USD complexes, USD NVs, or DOX NVs with normalized DOX concentrations. The IC_{50} values were obtained by fitting the cell viability against DOX concentrations. The USD complexes had an IC_{50} value of 0.237 μM which was slightly higher than that of free DOX (0.086 μM) on HCT116 cells (Fig. 4D). However, both USD NVs and DOX NVs showed less cytotoxicity to HCT 116 cells *in vitro* with IC_{50} values of 0.764 and 1.13 μM , respectively, according to the DOX concentration. Interestingly, the cytotoxicity of those DOX-containing formulations on A549 cells were significantly lower than those on HCT116 cells (Fig. S13), which could be due to the different internalization fate of those vesicular formulations on different cell lines. Further investigation on the cellular uptake efficacy and intracellular activity between those nanomaterials and different cell lines may help find out the underlying mechanism. Little to no toxicity to the HCT116 and A549 cells was found for both the USPIO NPs and blank NVs at a maximum concentration up to 160 $\mu\text{g}/\text{mL}$ on iron basis and 1000 $\mu\text{g}/\text{mL}$ on polymer weight, respectively (Fig. S14).

According to the present results, hereafter, we used HCT116 cells for further *in vitro* and *in vivo* studies. Flow cytometry assay results

indicated that the USD complexes and the USD NVs caused prominent apoptotic or necrotic cell death after 12 h incubation with HCT116 cells using Annex V R-PE and SYTOX Green co-staining method (Fig. S15). Compared with three parallel groups including blank control, USPIO NPs, and free DOX treatment with equivalent conditions, the USD complexes and the USD NVs treated cells had significantly higher percentages of early apoptotic cells (Q4) (Fig. S16). In addition, free DOX treatment induced the highest percentages of overall cell death, including apoptosis and necrosis (Q2 + Q4), among those of other groups. These results were consistent with the cytotoxicity assessment described in the MTT study.

Encouraged by the *in vitro* results, we further conducted cancer theranostic experiments *in vivo* using the USD NVs and with PBS, free DOX, US NVs, DOX NVs, and USD NVs + BSO as control groups ($n = 5/\text{group}$). After the tumor size reached around 40–50 mm^3 , we started the treatment through intravenous (i.v.) injection of each formula and repeated every three days for four times. Each dose represented 4 mg DOX per kg mouse body weight or equivalent components in different formulations. Three groups including USD NVs, US NVs, and USD NVs + BSO were further subjected to MRI acquisition before and after injection of each formulation. As shown in Fig. 5A–C, we acquired the pre-injection and post-injection (p.i.) MR images at 2, 6, 24, and 48 h p.i. for each mouse. The representative MR images of

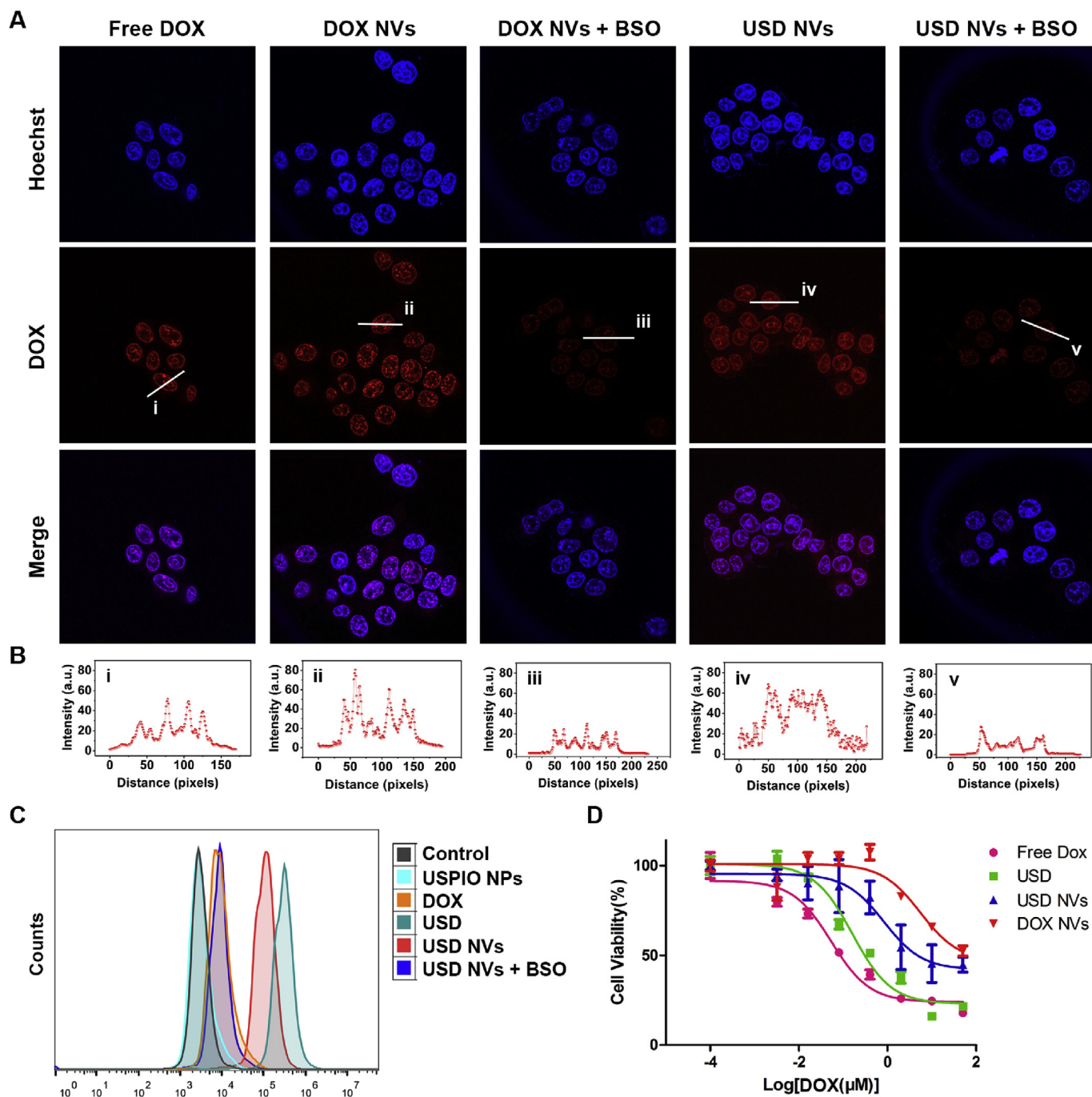


Fig. 4. *In vitro* cell studies of different formulations. (A) Confocal microscopy of HCT116 cells incubated with free DOX, DOX NVs, DOX NVs + BSO, USD NVs, and USD NVs + BSO for 2 h and were stained with Hoechst for acquisition. (B) Line profile analysis (white line in A, i-v) of the intensity of DOX in cell nucleus, indicating the different drug releasing efficacy in cells by different treatments. (C) Intracellular reactive oxygen species (ROS) generation treated with different formulations. (D) Cell viability curves of HCT116 cells treated with different formulations (48 h) with concentrations normalized to DOX contents.

mouse tumor injected with USD NVs showed enhanced bright contrast in the tumor region at 2 h p.i. which further increased at 6 and 24 h p.i. (Fig. 5A). These results indicated that the USD NVs were possibly decomposed by GSH stimulation, resulting in the dispersion of USPIO NPs dissociated from the clustering state. Meanwhile, it was conceivable that DOX molecules were dissociated from the USD complexes which might facilitate the anticancer activity. In this manner, drug release was concurrently accompanied by the T_1 MRI turn-on effect in the USD NVs which were able to monitor and evaluate the drug activity through noninvasive MRI. To investigate whether the decomposition of USD NVs is mediated by GSH, we further conducted the MRI study of mouse

treated with USD NVs + BSO (Fig. 5B). The MRI results showed little contrast enhancement in the T_1 images at 2, 6, 24, and 48 h p.i. time points compared with those of pre-contrast images. These results indicated that BSO treatment could reduce the efficacy of decomposition of USD NVs, probably due to the reduced tissue GSH level. Similar to the USD NVs, the US NVs show prominent T_1 bright contrast in mouse tumor especially for 6 and 24 h p.i. time points (Fig. 5C).

We further analyzed the T_1 MRI signal changes in mouse tumors with different treatments. Signal to noise ratio (SNR) of region-of-interest (ROI) tumor was analyzed according to the methods provided by the National Electrical Manufacturers Association (NEMA) standards

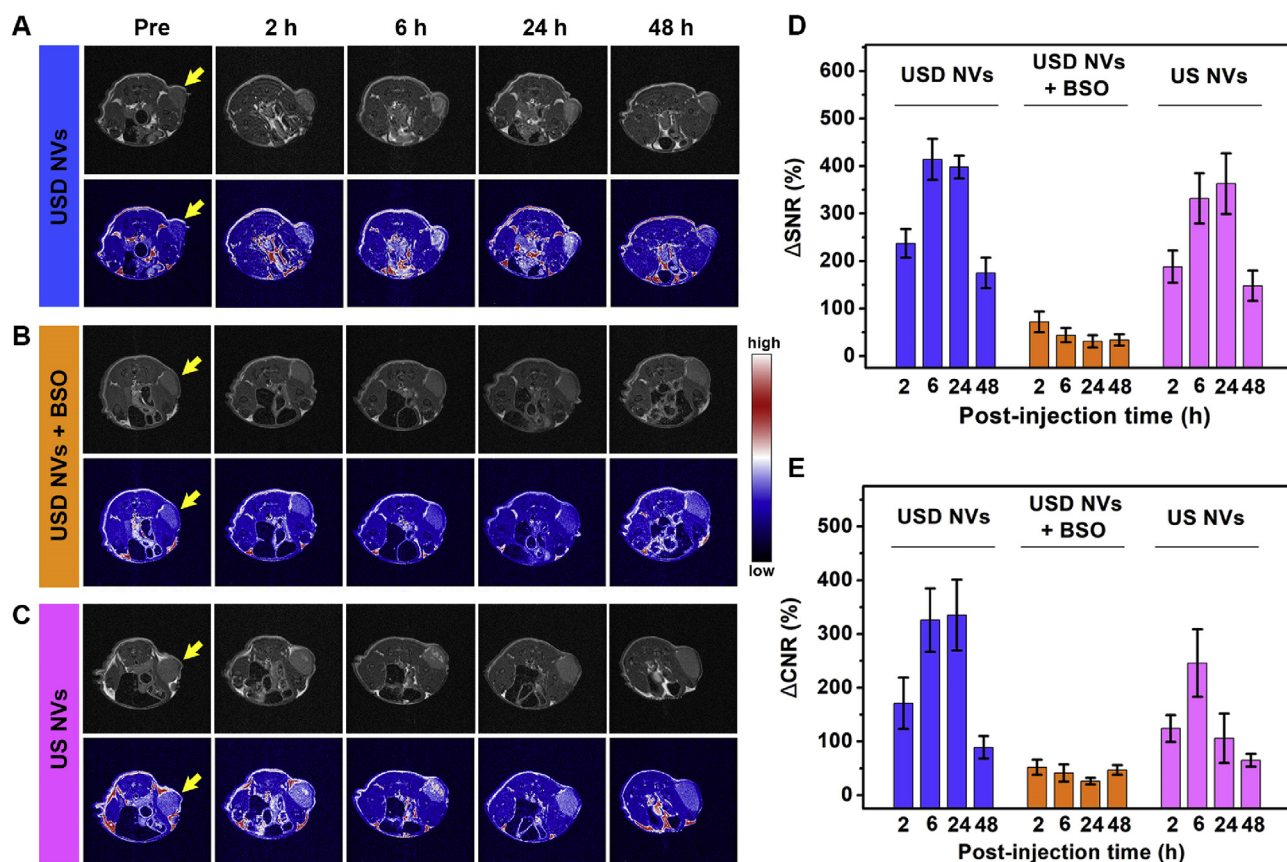


Fig. 5. *In vivo* MRI study of mouse treated with different formulations. (A–C) Transversal plane MRI (upper) and pseudo color images (lower) of tumor of mouse treated with USD NVs, USD NVs + BSO, and US NVs, respectively. Pre-injection (Pre) and 2, 6, 24, 48 h post-injection (p.i.) MRI were acquired accordingly. (D, E) Semiquantitative analysis of the signal changes Δ SNR and Δ CNR in tumor region by different treatments, respectively. (For interpretation of the references to color in this figure legend, the reader is referred to the Web version of this article.)

publication (MS 6–2008, R2014) on single-image measurement procedure for SNR. The following equations were used to calculate SNR and CNR of tumor: $SNR_{\text{tumor}} = SI_{\text{tumor}}/SD_{\text{noise}}$ (SI: signal intensity, SD: standard deviation); $CNR = |SNR_{\text{tumor}} - SNR_{\text{background}}|/SNR_{\text{tumor}}$; $\Delta SNR = |SNR_{\text{post}} - SNR_{\text{pre}}|/SNR_{\text{pre}}$; $\Delta CNR = |CNR_{\text{post}} - CNR_{\text{pre}}|/CNR_{\text{pre}}$. The results showed that Δ SNR at 6 and 24 h p.i. of mouse treated with USD NVs were about 10-fold greater than those of USD NVs + BSO, respectively (Fig. 5D). The gradual decrease of the Δ SNR at 48 h p.i. time point for both cases of the USD NVs and US NVs was probably due to the dissociation or metabolism (e.g., corona formation, agglomeration) of the USPIO NPs. The calculated Δ CNR showed similar trends as those of Δ SNR for mice treated with different formulations, respectively (Fig. 5E). Taken together, the USD NVs hold great promise in monitoring the drug release through GSH-mediated decomposition of the vesicular structure and a spatiotemporally concurrent activated T_1 MRI turn-on mechanism.

The anticancer activity of the USD NVs was evaluated by a four-time injection regimen every three days and the tumor size, mouse weight, survival rate were recorded every two days for each group (Fig. 6A). The tumor volumes were recorded until 20 days after the first treatment (Fig. 6B). The results showed that the USD NVs could significantly inhibit the mouse tumor growth compared with the control group ($***p < 0.001$). However, BSO treatment greatly reduced the anticancer potential of the USD NVs. This is probably due to the GSH mediated decomposition of USD NVs which greatly facilitates the burst release of DOX in tumor region. The tumor inhibition ratios at day 20 with respect to the control group were 12.3%, 28.3%, 53.1%, 59.4%, and 81.6% for the US NVs, free DOX, DOX NVs, USD NVs + BSO and USD NVs treated groups, respectively (Fig. 6C). Note that the mouse

group treated with free DOX suffered from severe body weight loss (10–15%), which was not observed in the other groups (Fig. S17). As a result, the mouse group treated with USD NVs had greatly improved survival rate compared with those of other groups (Fig. 6D). The terminal deoxynucleotidyl transferase dUTP nick end labeling (TUNEL) staining results of mouse tumors from different treatments (after four doses) further confirmed that the USD NVs treated mouse underwent highly prominent apoptotic cell death compared with other groups (Fig. 6E). Furthermore, the USD NVs and the DOX NVs exhibited greatly reduced cardiotoxicity, whereas the free DOX treated mice showed obvious cytoplasmic vacuolization and necrotic death of cardiomyocytes in heart tissue (Fig. 6F). Although the long-term toxicity of those formulations to major organs (liver, kidneys, spleen, and lung) were not obvious from H&E staining results (Fig. S18), DOX-induced cardiotoxicity and the ensuing cardiomyopathy is a major challenge in cancer therapy [63,64]. Our results indicate that the yolk-shell structure of the USD NVs can efficiently avoid DOX release during circulation, thereby sparing the toxicity to the cardiovascular systems.

4. Conclusions

In summary, we have developed a concurrent theranostic system based on GSH-responsive USD NVs in which both therapeutic drugs and diagnostic imaging agents were encapsulated and protected from activation. The easy formation of USD complexes between chemotherapeutic drugs and MRI contrast agents offers a convenient way of constructing MRI-guided cancer theranostics. The formed USD NVs showed great anticancer effect both *in vitro* and *in vivo* against HCT116, but not A549 tumor cells, probably due to the GSH mediated

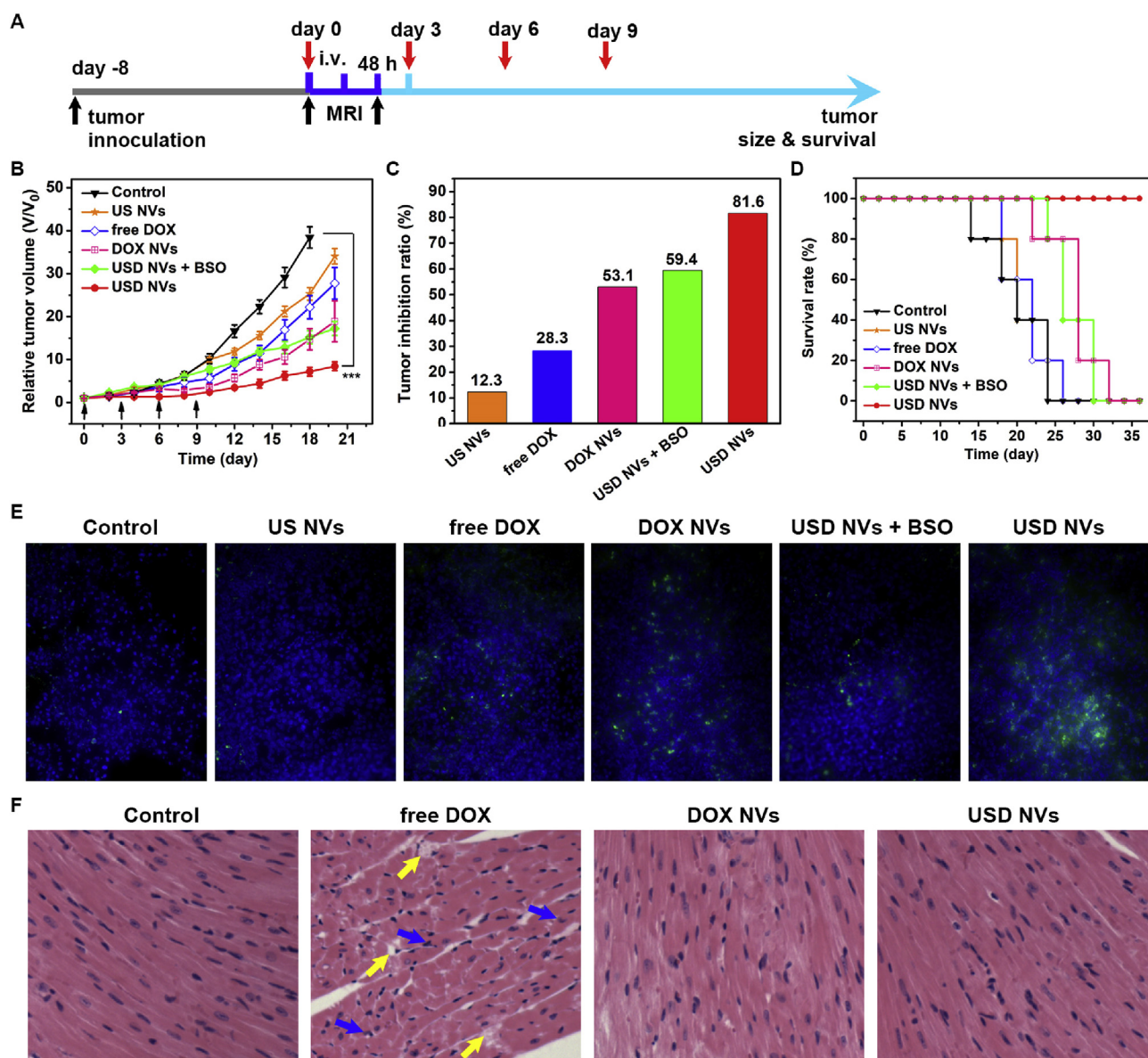


Fig. 6. *In vivo* anticancer study of the USD NVs. (A) Illustration of the anticancer study timeline. MRI is applied on selected groups (USD NVs, USD NVs + BSO, and US NVs) after the first injection for monitoring drug release and distribution. (B–D) Relative tumor volume changes, tumor inhibition ratios, and survival rate of mouse groups treated with different formulations, including PBS, free DOX, US NVs, DOX NVs, USD NVs + BSO and USD NVs. Black arrows indicate treatment timepoints (i.v.) with DOX content of 4 mg/kg mouse body weight. $***p < 0.001$. (E, F) Representative TUNEL staining images of mouse tumors and H&E staining images of mouse heart from different treatment groups, respectively. Yellow arrows indicate cytoplasmic vacuolization. Blue arrows indicate necrotic cell nucleus. (For interpretation of the references to color in this figure legend, the reader is referred to the Web version of this article.)

mechanism. More importantly, the USD NVs confer readily monitored drug release by the T_1 MRI activation in a spatiotemporally concurrent manner, which are amenable to report the drug activity and intratumoral distribution for improving the therapeutic efficacy and prognostic evaluation. This study provides a new paradigm of concurrent nanotheranostics by cooperating nanochemistry and MRI contrast mechanism, which may open up new avenues in the field of precision nanomedicine.

Declaration of competing interest

The authors declare no competing financial interests.

Acknowledgements

This work was supported by the Intramural Research Program (IRP),

National Institute of Biomedical Imaging and Bioengineering (NIBIB), National Institutes of Health (NIH), the National Natural Science Foundation of China (51761145021), Zhejiang Provincial Natural Science Foundation of China (R19E030002), Youth Innovation Promotion Association of the Chinese Academy of Sciences (2016269) (Z. S.). The author gratefully acknowledges financial support from China Scholarship Council (D. L.). The authors thank to Dr. Vincent Schram at the Microscopy Imaging Core (NIH) for technical support. The authors thank to Dr. Jeeva Munasinghe at the National Institute of Neurological Disorders and Stroke (NINDS) for MRI data acquisition.

Appendix A. Supplementary data

Supplementary data to this article can be found online at <https://doi.org/10.1016/j.biomaterials.2020.119979>.

References

- [1] Y. Wang, G. Giacccone, Challenges in cancer molecular targets and therapeutics, *Front Oncol* 1 (2011) 1–3.
- [2] J. Shi, P.W. Kantoff, R. Wooster, O.C. Farokhzad, Cancer nanomedicine: progress, challenges and opportunities, *Nat. Rev. Canc.* 17 (2016) 20.
- [3] G. Yu, X. Chen, Host-guest chemistry in supramolecular theranostics, *Theranostics* 9 (2019) 3041–3074.
- [4] W. Sun, Q. Hu, W. Ji, G. Wright, Z. Gu, Leveraging physiology for precision drug delivery, *Physiol. Rev.* 97 (2017) 189–225.
- [5] G. Bao, S. Mitragotri, S. Tong, Multifunctional nanoparticles for drug delivery and molecular imaging, *Annu. Rev. Biomed. Eng.* 15 (2013) 253–282.
- [6] W. Yang, Z. Zhou, J. Lau, S. Hu, X. Chen, Functional T cell activation by smart nanosystems for effective cancer immunotherapy, *Nano Today* 27 (2019) 28–47.
- [7] R. van der Meel, E. Sulheim, Y. Shi, F. Kiessling, W.J.M. Mulder, T. Lammers, Smart cancer nanomedicine, *Nat. Nanotechnol.* 14 (2019) 1007–1017.
- [8] D. Liu, F. Yang, F. Xiong, N. Gu, The smart drug delivery system and its clinical potential, *Theranostics* 6 (2016) 1306–1323.
- [9] H. Chen, W. Zhang, G. Zhu, J. Xie, X. Chen, Rethinking cancer nanotheranostics, *Nat Rev Mater* 2 (2017) 17024.
- [10] G. Yu, T.-Y. Cen, Z. He, S.-P. Wang, Z. Wang, X.-W. Ying, et al., Porphyrin nanocage-embedded single-molecular nanoparticles for cancer nanotheranostics, *Angew. Chem. Int. Ed.* 58 (2019) 8799–8803.
- [11] G. Yu, M. Zhang, M.L. Saha, Z. Mao, J. Chen, Y. Yao, et al., Antitumor activity of a unique polymer that incorporates a fluorescent self-assembled metallacycle, *J. Am. Chem. Soc.* 139 (2017) 15940–15949.
- [12] S.K. Golombok, J.-N. May, B. Theek, L. Appold, N. Drude, F. Kiessling, et al., Tumor targeting via EPR: strategies to enhance patient response, *Adv. Drug Deliv. Rev.* 130 (2018) 17–38.
- [13] D. Rosenblum, N. Joshi, W. Tao, J.M. Karp, D. Peer, Progress and challenges towards targeted delivery of cancer therapeutics, *Nat. Commun.* 9 (2018) 1410.
- [14] Y. Lu, A.A. Aimettil, R. Langer, Z. Gu, Bioresponsive materials, *Nat Rev Mater* 2 (2016) 16075.
- [15] K. Yang, L. Feng, Z. Liu, Stimuli responsive drug delivery systems based on nanographene for cancer therapy, *Adv. Drug Deliv. Rev.* 105 (2016) 228–241.
- [16] W. Gao, J.M. Chan, O.C. Farokhzad, pH-responsive nanoparticles for drug delivery, *Mol. Pharm.* 7 (2010) 1913–1920.
- [17] W. Wu, L. Luo, Y. Wang, Q. Wu, H.-B. Dai, J.-S. Li, et al., Endogenous pH-responsive nanoparticles with programmable size changes for targeted tumor therapy and imaging applications, *Theranostics* 8 (2018) 3038–3058.
- [18] Y. Guo, Y. Ran, Z. Wang, J. Cheng, Y. Cao, C. Yang, et al., Magnetic-responsive and targeted cancer nanotheranostics by PA/MR bimodal imaging-guided photo-thermally triggered immunotherapy, *Biomaterials* 219 (2019) 119370.
- [19] Q. Sun, H. Bi, Z. Wang, C. Li, X. Wang, J. Xu, et al., Hyaluronic acid-targeted and pH-responsive drug delivery system based on metal-organic frameworks for efficient antitumor therapy, *Biomaterials* 223 (2019) 119473.
- [20] X. Ling, J. Tu, J. Wang, A. Shajii, N. Kong, C. Feng, et al., Glutathione-responsive prodrug nanoparticles for effective drug delivery and cancer therapy, *ACS Nano* 13 (2019) 357–370.
- [21] D.C. Thang, Z. Wang, X. Lu, B. Xing, Precise cell behaviors manipulation through light-responsive nano-regulators: recent advance and perspective, *Theranostics* 9 (2019) 3308–3340.
- [22] Y. Liu, Z. Yang, X. Huang, G. Yu, S. Wang, Z. Zhou, et al., Glutathione-responsive self-assembled magnetic gold nanowreath for enhanced tumor imaging and imaging-guided photothermal therapy, *ACS Nano* 12 (2018) 8129–8137.
- [23] N. Yan, L. Lin, C. Xu, H. Tian, X. Chen, A GSH-gated DNA nanodevice for tumor-specific signal amplification of microRNA and MR imaging-guided theranostics, *Small* 15 (2019) 1903016.
- [24] T. Lammers, L.Y. Rizzo, G. Storm, F. Kiessling, Personalized nanomedicine, *Clin. Canc. Res.* 18 (2012) 4889–4894.
- [25] X. Zhu, J. Li, P. Peng, N. Hosseini Nassab, B.R. Smith, Quantitative drug release monitoring in tumors of living subjects by magnetic particle imaging nanocomposite, *Nano Lett.* 19 (2019) 6725–6733.
- [26] K. Li, Q. Su, W. Yuan, B. Tian, B. Shen, Y. Li, et al., Ratiometric monitoring of intracellular drug release by an upconversion drug delivery nanosystem, *ACS Appl. Mater. Interfaces* 7 (2015) 12278–12286.
- [27] J. Song, L. Lin, Z. Yang, R. Zhu, Z. Zhou, Z.-W. Li, et al., Self-assembled responsive bilayered vesicles with adjustable oxidative stress for enhanced cancer imaging and therapy, *J. Am. Chem. Soc.* 141 (2019) 8158–8170.
- [28] Y. Liu, C.S. Gong, Y. Dai, Z. Yang, G. Yu, Y. Liu, et al., In situ polymerization on nanoscale metal-organic frameworks for enhanced physiological stability and stimulus-responsive intracellular drug delivery, *Biomaterials* 218 (2019) 119365.
- [29] A. Ma, H. Chen, Y. Cui, Z. Luo, R. Liang, Z. Wu, et al., Metalloporphyrin complex-based nanosensitizers for deep-tissue tumor theranostics by noninvasive sonodynamic therapy, *Small* 15 (2019) 1804028.
- [30] K.Y. Choi, G. Liu, S. Lee, X. Chen, Theranostic nanoplatforams for simultaneous cancer imaging and therapy: current approaches and future perspectives, *Nanoscale* 4 (2012) 330–342.
- [31] S. Kunjachan, J. Ehling, G. Storm, F. Kiessling, T. Lammers, Noninvasive imaging of nanomedicines and nanotheranostics: principles, progress, and prospects, *Chem. Rev.* 115 (2015) 10907–10937.
- [32] E.K.-H. Chow, D. Ho, Cancer nanomedicine: from drug delivery to imaging, *Sci. Transl. Med.* 5 (2013) 216rv4-rv4.
- [33] Z. Zhou, A. Chan, Z. Wang, X. Huang, G. Yu, O. Jacobson, et al., Synchronous chemoradiation nanovesicles by X-ray triggered cascade of drug release, *Angew. Chem. Int. Ed.* 57 (2018) 8463–8467.
- [34] Y. Min, J.M. Caster, M.J. Eblan, A.Z. Wang, Clinical translation of nanomedicine, *Chem. Rev.* 115 (2015) 11147–11190.
- [35] M. Qiu, D. Wang, W. Liang, L. Liu, Y. Zhang, X. Chen, et al., Novel concept of the smart NIR-light-controlled drug release of black phosphorus nanostructure for cancer therapy, *Proc. Natl. Acad. Sci. U. S. A.* 115 (2018) 501–506.
- [36] L. Tang, Z. Yang, Z. Zhou, Y. Ma, D.O. Kiesewetter, Z. Wang, et al., A logic-gated modular nanovesicle enables programmable drug release for on-demand chemotherapy, *Theranostics* 9 (2019) 1358–1368.
- [37] L. Zhou, H. Wang, Y. Li, Stimuli-responsive nanomedicines for overcoming cancer multidrug resistance, *Theranostics* 8 (2018) 1059–1074.
- [38] M. Satpathy, L. Wang, R.J. Zielinski, W. Qian, Y.A. Wang, A.M. Mohs, et al., Targeted drug delivery and image-guided therapy of heterogeneous ovarian cancer using HER2-targeted theranostic nanoparticles, *Theranostics* 9 (2019) 778–795.
- [39] C. Moore, J.V. Jokerst, Strategies for image-guided therapy, surgery, and drug delivery using photoacoustic imaging, *Theranostics* 9 (2019) 1550–1571.
- [40] H. Zhao, G. Shu, J. Zhu, Y. Fu, Z. Gu, D. Yang, Persistent luminescent metal-organic frameworks with long-lasting near infrared emission for tumor site activated imaging and drug delivery, *Biomaterials* 217 (2019) 119332.
- [41] M.L. Viger, J. Sankaranarayanan, C. de Gracia Lux, M. Chan, A. Almutairi, Collective activation of MRI agents via encapsulation and disease-triggered release, *J. Am. Chem. Soc.* 135 (2013) 7847–7850.
- [42] E. Rideau, R. Dimova, P. Schuille, W. Krum, K. Landfester, Liposomes and polymersomes: a comparative review towards cell mimicking, *Chem. Soc. Rev.* 47 (2018) 8572–8610.
- [43] F. De Sarno, A.M. Ponsiglione, M. Russo, A.M. Grimaldi, E. Forte, P.A. Netti, et al., Water-mediated nanostructures for enhanced MRI: impact of water dynamics on relaxometric properties of Gd-DTPA, *Theranostics* 9 (2019) 1809–1824.
- [44] J. Wahsner, E.M. Gale, A. Rodríguez-Rodríguez, P. Caravan, Chemistry of MRI contrast agents: current challenges and new frontiers, *Chem. Rev.* 119 (2019) 957–1057.
- [45] E.J. Werner, A. Datta, C.J. Jocher, K.N. Raymond, High-relaxivity MRI contrast agents: where coordination chemistry meets medical imaging, *Angew. Chem. Int. Ed.* 47 (2008) 8568–8580.
- [46] Z. Zhou, Z. Zhao, H. Zhang, Z. Wang, X. Chen, R. Wang, et al., Interplay between longitudinal and transverse contrasts in Fe₃O₄ nanoplates with (111) exposed surfaces, *ACS Nano* 8 (2014) 7976–7985.
- [47] V.C. Pierre, S.M. Harris, S.L. Pailloux, Comparing strategies in the design of responsive contrast agents for magnetic resonance imaging: a case study with copper and zinc, *Acc. Chem. Res.* 51 (2018) 342–351.
- [48] Z. Zhou, L. Yang, J. Gao, X. Chen, Structure-relaxivity relationships of magnetic nanoparticles for magnetic resonance imaging, *Adv. Mater.* 31 (2019) 1804567.
- [49] Z. Zhou, R. Tian, Z. Wang, Z. Yang, Y. Liu, G. Liu, et al., Artificial local magnetic field inhomogeneity enhances T₂ relaxivity, *Nat. Commun.* 8 (2017) 15468.
- [50] F. Li, Z. Liang, J. Liu, J. Sun, X. Hu, M. Zhao, et al., Dynamically reversible iron oxide nanoparticle assemblies for targeted amplification of T₁-weighted magnetic resonance imaging of tumors, *Nano Lett.* 19 (2019) 4213–4220.
- [51] D. Ni, W. Bu, E.B. Ehlerting, W. Cai, J. Shi, Engineering of inorganic nanoparticles as magnetic resonance imaging contrast agents, *Chem. Soc. Rev.* 46 (2017) 7438–7468.
- [52] W. Ong, Y. Yang, A.C. Cruciano, R.L. McCarley, Redox-triggered contents release from liposomes, *J. Am. Chem. Soc.* 130 (2008) 14739–14744.
- [53] Z. Shen, T. Chen, X. Ma, W. Ren, Z. Zhou, G. Zhu, et al., Multifunctional theranostic nanoparticles based on exceedingly small magnetic iron oxide nanoparticles for T₁-weighted magnetic resonance imaging and chemotherapy, *ACS Nano* 11 (2017) 10992–11004.
- [54] A. Napoli, M. Valentini, N. Tirelli, M. Muller, J.A. Hubbell, Oxidation-responsive polymeric vesicles, *Nat. Mater.* 3 (2004) 183–189.
- [55] K. Lv, Q. Li, L. Zhang, Y. Wang, Z. Zhong, J. Zhao, et al., Incorporation of small extracellular vesicles in sodium alginate hydrogel as a novel therapeutic strategy for myocardial infarction, *Theranostics* 9 (2019) 7403–7416.
- [56] S. Wang, L. Yang, H.-Y. Cho, S.-T. Dean Chueng, H. Zhang, Q. Zhang, et al., Programmed degradation of a hierarchical nanoparticle with redox and light responsiveness for self-activated photo-chemical enhanced chemodynamic therapy, *Biomaterials* 224 (2019) 119498.
- [57] B.H. Kim, N. Lee, H. Kim, K. An, Y.I. Park, Y. Choi, et al., Large-scale synthesis of uniform and extremely small-sized iron oxide nanoparticles for high-resolution T₁ magnetic resonance imaging contrast agents, *J. Am. Chem. Soc.* 133 (2011) 12624–12631.
- [58] H. Wei, O.T. Bruns, M.G. Kaul, E.C. Hansen, M. Barch, A. Wisniewska, et al., Exceedingly small iron oxide nanoparticles as positive MRI contrast agents, *Proc. Natl. Acad. Sci. U. S. A.* 114 (2017) 2325–2330.
- [59] M. Feng, Y. Yang, P. He, Y. Fang, Spectroscopic studies of copper(II) and iron(II) complexes of adriamycin, *Spectrochim. Acta Mol. Biomol. Spectrosc.* 56 (2000) 581–587.
- [60] K.D. Mjos, J.F. Cawthray, G. Jamieson, J.A. Fox, C. Orvig, Iron(III)-binding of the anticancer agents doxorubicin and vorosaron, *Dalton Trans.* 44 (2015) 2348–2358.
- [61] H.-K. Liu, P.J. Sadler, Metal complexes as DNA intercalators, *Acc. Chem. Res.* 44 (2011) 349–359.
- [62] C. Sun, L. Wang, B. Xianyu, T. Li, S. Gao, H. Xu, Selenoxide elimination manipulate the oxidative stress to improve the antitumor efficacy, *Biomaterials* 225 (2019) 119514.
- [63] X. Wu, Y. Zhu, W. Huang, J. Li, B. Zhang, Z. Li, et al., Hyperbaric oxygen potentiates Doxil antitumor efficacy by promoting tumor penetration and sensitizing cancer cells, *Adv. Sci.* 5 (2018) 1700859.
- [64] Y. He, X. Li, J. Ma, G. Ni, G. Yang, S. Zhou, Programmable codelivery of doxorubicin and apatinib using an implantable hierarchical-structured fiber device for overcoming cancer multidrug resistance, *Small* 15 (2019) 1804397.